

Available online at www.sciencedirect.com



journal homepage: www.elsevier.com/locate/jmrt



Modeling the multiaxial fracture behavior of Ti-6Al-4V alloy sheets at a high temperature using improved damage modeling



Jinwoo Lee ^a, Hyuk Jong Bong ^{b,**}, Daeyong Kim ^c, Jinjin Ha ^{d,*}

- ^a School of Mechanical Engineering, University of Ulsan, Ulsan, 44610, Republic of Korea
- ^b Department of Materials Processing, Korea Institute of Materials Science, Changwon, 51508, Republic of Korea
- ^c Department of Intelligent Mobility, Chonnam National University, Gwangju, 61186, Republic of Korea
- ^d Department of Mechanical Engineering, University of New Hampshire, Durham, NH, 03824, USA

ARTICLE INFO

Article history: Received 19 March 2023 Accepted 6 June 2023 Available online 9 June 2023

Keywords:
Titanium alloys
Hot deformation
Constitutive modeling
Damage model
Finite element

ABSTRACT

In this study, the mechanical responses of Ti-6Al-4V alloy sheets at a high temperature under multi-axial loading were investigated using a micromechanics-based damage model within a continuum finite element (FE) framework. Tensile tests at three strain rates and a high temperature were conducted to analyze the plastic and ductile damage properties of the Ti-6Al-4V alloy sheets. Additionally, hot Nakajima tests were conducted on specimens with three different shapes to evaluate the improvement in formability at a high temperature. Moreover, the dimples on the fractured surfaces of the experimental samples were qualitatively analyzed. Simultaneously, corresponding FE simulations were conducted to predict the ductile damage behavior of the Ti-6Al-4V alloy sheets at a high temperature using a modified Gurson-Tvergaard-Needleman model. The predicted results and the displacements at the onset of failure were compared with the corresponding experimental data.

Published by Elsevier B.V. This is an open access article under the CC BY-NC-ND license (http://creativecommons.org/licenses/by-nc-nd/4.0/).

1. Introduction

Titanium alloys have been used for producing structural parts of aircraft for over a century owing to the corrosion resistance, high strength, and low weight of these alloys [1]. More specifically, Ti–6Al–4V alloy sheets have recently received considerable attention for high-performance applications in the aircraft industry [2]. However, the major drawbacks of Ti–6Al–4V alloy sheets are low formability and high spring back at room temperature [3]. Therefore, high-temperature-

assisted forming processes, such as hot forming (HF) and superplastic forming (SPF) technologies, must be developed for Ti–6Al–4V alloy sheets [4]. Furthermore, SPF has been conducted on Ti–6Al–4V alloy sheets at high temperatures, such as over 800 $^{\circ}$ C, to manufacture parts with substantially improved formability. However, several technical obstacles, such as high energy consumption to increase temperature and low production speed, remain. The forming temperature applied to Ti–6Al–4V alloy sheets in the HF process (less than 800 $^{\circ}$ C) is lower than that applied in the SPF process and a hydraulic press machine is used in the HF process, thereby

E-mail addresses: hjbong@kims.re.kr (H.J. Bong), Jinjin.Ha@unh.edu (J. Ha).

^{*} Corresponding author.

^{**} Corresponding author.

increasing productivity. Identifying the optimal forming temperature used in the HF process and the corresponding material behavior of Ti-6Al-4V alloy sheets may improve the quality of the product manufactured via this process.

A previous experimental study [5] revealed that the microstructure of Ti-6Al-4V alloys changed drastically when they were heated to temperatures over 750 °C. Furthermore, Ti-6Al-4V alloy sheets are composed of an α -phase (hexagonal-closest-packed structure) and a β-phase (body-centeredcubic structure) at room temperature [6]. After the HF process, additional stresses, such as residual stress, in the Ti-6Al-4V alloys should be relieved at a temperature range of 480-650 °C to reduce the amount of spring back and prevent stressinduced corrosion and crack propagation [1,7]. However, Ti-6Al-4V alloys usually undergo oxidation at temperatures exceeding 480 °C, thereby resulting in the formation of hard and brittle oxygen-enriched layers, which are known as α case layers, on the surface [8]. The α -case layer results in poor properties such as reduced formability and fatigue life of the Ti-6Al-4V alloy product. A thin α -case layer can be observed when Ti-6Al-4V alloys are heated for over 50 h at 650 °C [9,10].

The dominant factors affecting the plastic deformation and ductile damage behaviors of Ti-6Al-4V alloys are temperature, strain rate, and strain path under high-temperature forming conditions [11–16]. Additionally, extensive studies have been conducted to investigate the relationship between the microstructures and mechanical behaviors of Ti-6Al-4V alloys at HF temperatures. Paghandeh et al. [17-20] analyzed the flow stress behavior and corresponding microstructural evolution of Ti-6Al-4V alloys and the effect of the initial microstructure on the ductility of these alloys. Ti-6Al-4V alloys can dynamically recrystallize during plastic deformation at low strain rates and a temperature range of 650-750 °C, resulting in a flow softening behavior caused by microstructural changes [21]. Consequently, the optimal forming temperature of Ti-6Al-4V alloy sheets under the HF process is approximately 650 °C, at which dynamic recrystallization is not dominant but the good formability of the alloys is maintained.

Coupled plasticity-damage models constructed via micromechanics-based damage modeling have been widely used in metal-forming processes [22–24]. Particularly, the series of Gurson-Tvergaard-Needleman (GTN) models [25–27] has provided valuable physical insights into the ductile damage behaviors of metals in terms of void growth, nucleation, and coalescence. GTN models assume a uniform distribution of spherical voids in metals and use the volume fraction of these voids as an internal damage variable. Although these models can reproduce the mechanical behaviors of polycrystalline metals at high-stress triaxiality [28–34], they cannot address damage behaviors at low-stress triaxiality [35,36]. Therefore, in the last few decades, several studies have been conducted to overcome the aforementioned

limitations and improve the applicability of GTN models. For example, additional state variables have been implemented [37–41], and arbitrary elliptical voids have been considered in ductile metals, leading to improved predictive accuracy at low-stress triaxiality [42–48]. Alternatively, the uncoupled phenomenological ductile fracture model has also been applied to predict material failure regardless of the microstructural evolution during plastic deformation [49].

To date, few attempts have been made to model the mechanical behaviors of Ti-6Al-4V alloy sheets at high temperatures under multi-axial loading conditions. Previous studies mostly focused on the mechanical responses of Ti-6Al-4V alloys at moderate temperatures under monotonic loading [4,11,50-53]. Bong et al. [54] conducted multi-axial loading experiments on Ti-6Al-4V alloy sheets at high temperatures and systematically characterized the mechanical responses of these sheets. The authors observed improved formability at high temperatures. Furthermore, previous studies [54] revealed that GTN models can capture the hot deformation behaviors under the monotonic tension and balanced biaxial stretch deformation modes of Ti-6Al-4V alloy sheets; however, large deviations were observed between the simulated and experimental uniaxial stretch and plane strain stretch deformation modes under hightemperature conditions. To the best of the authors' knowledge, there has been a lack of comprehensive research on material modeling of Ti-6Al-4V alloy sheets at high temperatures. Therefore, the complex deformation behavior of Ti-6Al-4V alloy sheets must be rigorously modeled to improve the prediction accuracy under high-temperature conditions.

The objective of this study is to improve material modeling using finite element (FE) simulations in to accurately capture the ductile damage behavior of Ti-6Al-4V alloy sheets that are subjected to various loading conditions at high temperatures. The formability and damage behavior at high temperatures were evaluated by performing hot uniaxial tension tests and hot Nakajima tests under multi-axial loading consimulations, including plasticity micromechanics-based damage models, were implemented. Subsequently, the simulation results were compared with the experimental results. Section 2 presents the experimental results of the hot uniaxial tension and hot Nakajima tests. The hot Nakajima tests evaluated the plastic deformation of three sample specimens subjected to different deformation modes under multi-axial loading conditions. In Section 3, the modeled plasticity and ductile damage behaviors of the materials are described. The plasticity model was proposed to capture flow softening and isotropic plastic-yielding properties. The Gurson-type micromechanics-based damage model was used to perform the numerical simulations. Section 4 presents the comparison between the numerical and experimental results obtained from the hot uniaxial tension and hot Nakajima tests. Furthermore, the fractographic analysis of the

Table 1 $-$ Chemical composition of the Ti $-$ 6Al $-$ 4V alloy sheets (unit: wt%).									
Al	V	С	N	0	Н	Fe	Y	Ti	
5.5-6.75	3.5-4.5	≤0.08	≤0.05	≤0.2	≤0.0125	≤0.3	≤0.005	Bal.	

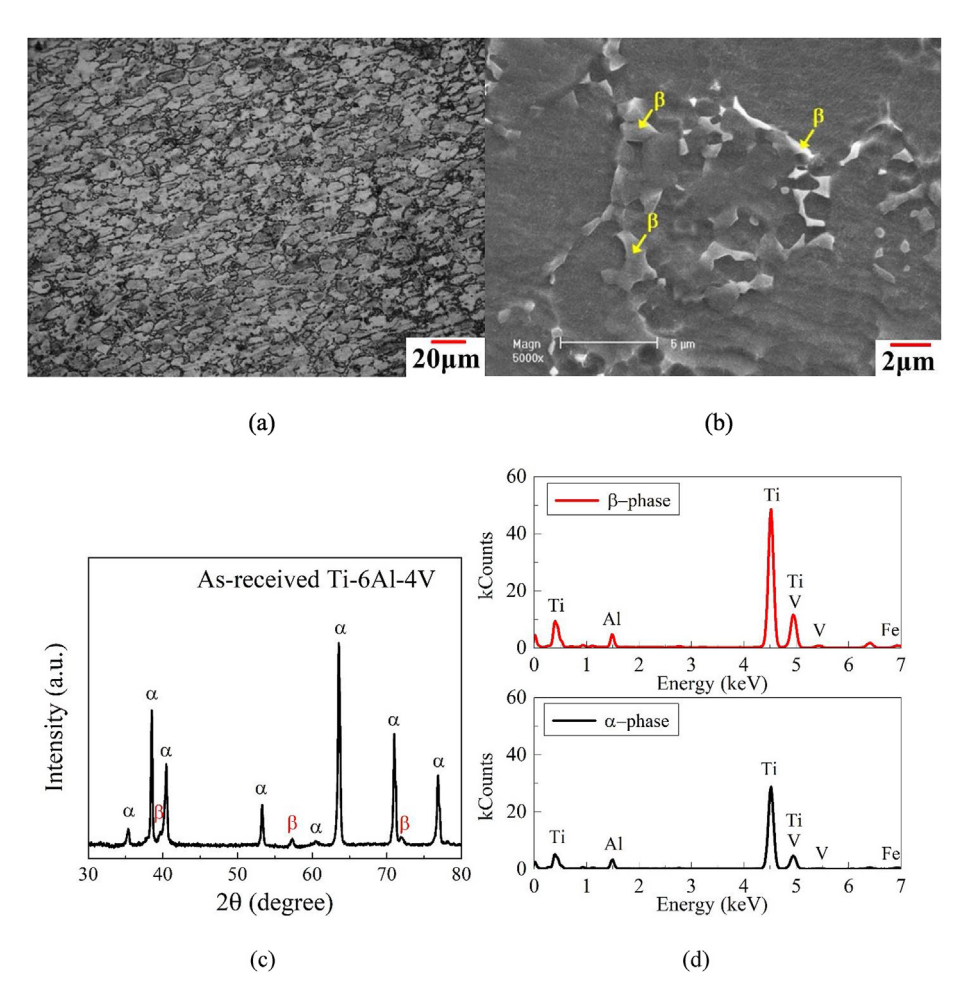


Fig. 1 – (a) OM and (b) SEM images, (c) X-ray diffraction patterns, and (d) EDS analysis of as-received Ti-6Al-4V alloy sheets [54,56].

fracture surface is discussed. Finally, in Section 5, the summary and conclusions of this study are presented.

2. Experimental procedure

2.1. Material

Sheets of mill-annealed Ti-6Al-4V alloy with a thickness of 1.27 mm (0.05 in) were used in this study. The chemical

composition of the material is provided in Table 1. The optical microscope (OM, MA200, Nikon, Japan) image of the asreceived material is shown in Fig. 1 (a), and the material consists of an α -phase matrix and a small volume fraction of β -phase particles [6,55]. A scanning electron microscope (SEM) (JS-7600F, FE-SEM, JEOL, Japan) was used to analyze the microstructures of the samples, as shown in Fig. 1 (b). The SEM image reveals that the average grain size of the α -phase matrix was 10 μ m, and the β -phase particles were positioned at the grain boundaries of the α -phase matrix [54,56]. The X-ray

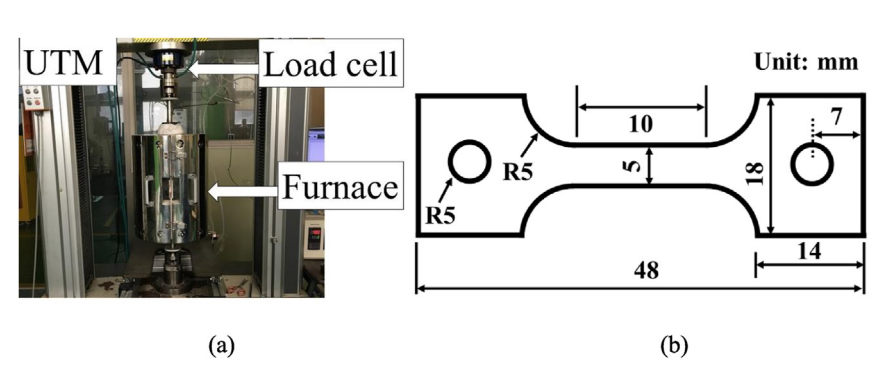


Fig. 2 - (a) Universal testing machine with a furnace heating system, and the (b) shape and dimensions of the specimens under monotonic loading at a high temperature [56].

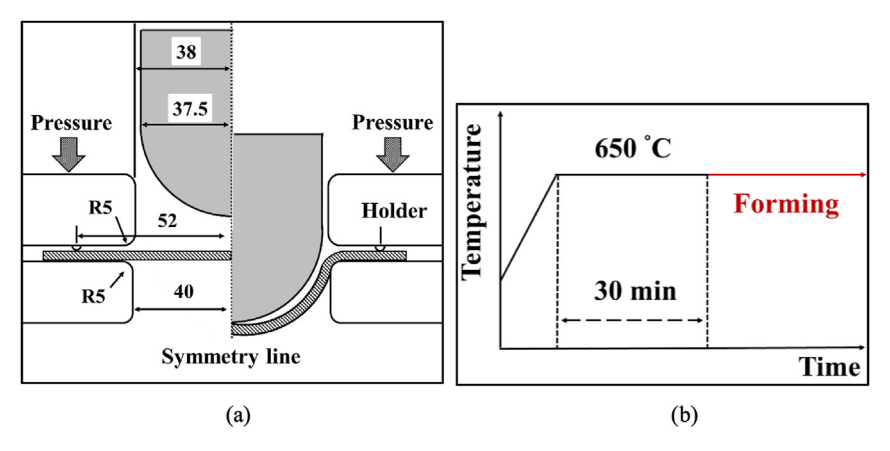


Fig. 3 – (a) Schematic view of the hot Nakajima test, and (b) temperature history of the specimen sample during the hot Nakajima tests [54].

diffraction patterns, and the EDS analysis obtained from the as-received material are displayed Fig. 1 (c) and (d), respectively. Furthermore, the representative fracture surfaces after the mechanical tests were observed using the SEM.

2.2. Monotonic loading tests at high temperatures

Uniaxial tension experiments were performed in accordance with ASTM E21 [57] using a universal testing machine (UTM, MINOS-100, MTDI, Korea) equipped with a furnace heating system. Fig. 2 (a) displays the UTM, which consists of a load cell, furnace heating system, and heatproof plate between the load cell and furnace. The air temperature inside the furnace was increased up to the target temperature of 650 °C, the tensile specimens were placed inside the furnace for 1 h, and a uniform temperature distribution was maintained in the specimens. The specimen geometry is shown in Fig. 2 (b) with a gauge length of 10 mm. A cross-head speed of 5×10^{-2} mm/s, equivalent to a strain rate of 5×10^{-3} /s, was applied. The load was measured using the load cell, and the displacement of the specimen was assumed to be equivalent to the cross-head stroke of the UTM [56]. At least three tests were conducted to confirm the repeatability of the results, and the samples were placed along the rolling direction under hightemperature conditions during the uniaxial tension tests.

2.3. Multiaxial loading tests at a high temperature

The hot Nakajima tests on the Ti-6Al-4V alloy sheets under multiaxial deformations were conducted in accordance with ISO 12004-2 [58]. The testing tools consisted of a die, punch, and holder and were installed in the UTM, which is capable of measuring a maximum load of 10 kN [54]. In addition, the electric furnace heating system was equipped to maintain a uniform temperature distribution, and all tools were placed inside it. The temperature inside the furnace was raised to 650 °C and maintained for one day before conducting the experiments. Fig. 3 (a) illustrates the detailed dimensions of the equipment used in the hot Nakajima tests. A hemispherical punch with a radius of 37.5 mm was used, and the diameters of the holder and die were 76 and 80 mm, respectively. A lock bead with a diameter of 104 mm was built into the holder to hold the specimen samples during the test. The specimen samples were placed on the die for 30 min and then clamped by the holder with a holding pressure of 8 MPa. The punch speed was 0.5 mm/ s under an approximately quasi-static condition. Additionally, a boron nitride lubricant was used on the sample surfaces in contact with the tools to eliminate friction. The punch load and displacement were recorded during the test, and the temperature history of the sample is shown in Fig. 3 (b).

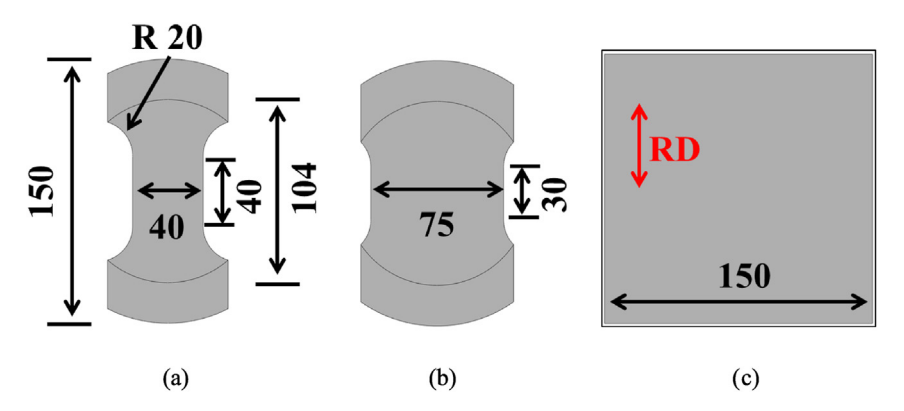


Fig. 4 — Specimen geometries and dimensions used in the hot Nakajima test at 650 $^{\circ}$ C subjected to (a) uniaxial-stretch (W40), (b) plane-strain (W75), and (c) biaxial-stretch (W150) deformation modes (Unit: mm).

Specimen samples with various shapes were used in the hot Nakajima tests under multiaxial loading, as shown in Fig. 4. Three geometries with different minimum specimen widths were used, and the specimens correspond to the uniaxial stretch (W40), plane-strain (W75), and biaxial stretch (W150) deformations. The deformation path of each specimen was confirmed via FE simulations [56]. The rolling direction was used as the major loading direction of the specimen sample. A 1-mm-diameter circular grid pattern at 2-mm intervals between the centers of adjacent grids was chemically etched onto the surfaces of the specimen samples [59–61], and the strain distributions on these surfaces were measured using the ARGUS optical strain measuring system after conducting the experiments.

3. Numerical simulations – constitutive models and finite element modeling

3.1. Constitutive modeling of plastic deformation

The plastic flow curves, including the strain-rate sensitivity effect, were reproduced according to the following empirical equation [62,63]:

$$\sigma_{\rm IH} = \sigma(\bar{\epsilon}, \dot{\epsilon}) = \sigma_{\rm f}(\bar{\epsilon}) \cdot \sigma_{\rm g}(\dot{\epsilon})$$
 (1)

where σ_{IH} , $\bar{\epsilon}$, and $\dot{\epsilon}$ represent the monotonic stress, equivalent plastic strain, and strain rate, respectively. Additionally, functions σ_f and σ_g represent the strain hardening at a reference strain rate and strain-rate dependent hardening, respectively.

In this study, the Voce hardening law and power law-type function were adopted to construct the reference flow curve. Additionally, $\sigma_f(\bar{\epsilon})$ was modeled using either Voce hardening or the power law-type function as follows [56]:

$$\sigma_{f}(\overline{\epsilon}) = A + B(1 - e^{-C\overline{\epsilon}}) \tag{2}$$

$$\sigma_{g}(\dot{\varepsilon}) = \left(\frac{\dot{\varepsilon}}{\dot{\varepsilon}_{0}}\right)^{m} \tag{3}$$

where A, B, C, and m are material constants to be fitted using the plastic flow curves under uniaxial tension and $\dot{\epsilon}_0$ is the reference strain rate.

In addition, the flow stress softening of the Ti-6Al-4V alloy sheets, resulting from dynamic recrystallization at a high temperature, was described using a softening factor added in the following exponential form [64,65]:

$$\sigma_{s}(\overline{\epsilon}) = p + (1 - p)e^{-q\overline{\epsilon}^{r}}$$
(4)

where p, q, and r are the material coefficients fitted using the hardening deterioration behavior under uniaxial tension. Material constant p is assumed to be linear with respect to the strain rate as follows:

$$p(\dot{\varepsilon}) = p_0 \cdot (\dot{\varepsilon} - \dot{\varepsilon}_0) + p_1 \tag{5}$$

where p_0 and p_1 are material coefficients. As reported in the literature [65,66], the flow stress deterioration is affected by the temperature and loading rate associated with dynamic recrystallization; therefore, the relationship between the

softening factor and strain rate can be reasonably assumed to

Consequently, the plastic flow stress σ_{IH} was reproduced based on the following empirical equation:

$$\sigma_{IH} = \sigma(\overline{\epsilon}, \dot{\epsilon}) = \sigma_f(\overline{\epsilon}) \cdot \sigma_g(\dot{\epsilon}) \cdot \sigma_s(\overline{\epsilon}, \dot{\epsilon}) \tag{6}$$

3.2. Constitutive modeling of ductile damage

In this study, the Gurson-type damage model was applied to describe the ductile damage and fracture behavior at a high temperature under multi-axial loading. Originally, Gurson [25] developed a constitutive equation of a porous material that consisted of spherical voids surrounded by a material matrix, and the model could reproduce the nucleation and growth of these voids during inelastic deformation by changing the volume fraction of the voids. Later, Tvergaard and Needleman [26] reformulated the Gurson model to include the coalescence of voids during plastic deformation. The basic equation of the Gurson-type model is expressed as:

$$\Phi(\sigma) = \underbrace{\left(\frac{\overline{\sigma}}{\sigma_{IH}}\right)^{2} - 1}_{Plasticity} + \underbrace{2q_{1}f_{*} \cosh\left(q_{2}\frac{3p}{2\sigma_{IH}}\right) - q_{3}f_{*}^{2}}_{Effect of voids} = 0$$
 (7)

where \overline{o} is the von-Mises effective stress; $\sigma_{\rm IH}$ is the flow stress of the fully dense matrix material defined in Eq. (6); p is a hydrostatic pressure; f_* is a function of the void volume fraction f_* ; and q_1 , q_2 , and q_3 are material coefficients. The recommended values of the material coefficients of metals are $q_1=1.0-1.5$, $q_2=1.0$, and $q_3=(q_1)^2$ [26]. The values applied for the Ti-6Al-4V alloy sheets in this study were $q_1=1.5$, $q_2=1.0$, and $q_3=2.25$ investigated in this study. The function f_* accounts for the loss of stiffness during plastic deformation and is expressed as:

$$f_{*} = \begin{cases} f \\ f_{c} + \frac{f_{u} - f_{c}}{f_{f} - f_{c}} (f - f_{c}) & \text{if } f_{c} \leq f \leq f_{f} \\ f_{t} & \text{f.} \end{cases}$$
 (8)

where f_c is the critical volume fraction of the voids, f_f is the volume fraction of the voids at the onset of material failure, and f_u is the value of the function when the stiffness of the material completely disappears and is computed as

$$f_u = \frac{q_1 + \sqrt{q_1^2 - q_3}}{q_3} \tag{9}$$

The total volume fraction of the voids evolves as follows:

$$df = df_{\rm n} + df_{\rm g} + df_{\rm s} \tag{10}$$

where df_n and df_g are the increments of the void volume due to new void nucleation and growth, respectively. The additional factor, df_s , is the increment of the void volume depending on the loading direction.

The change in void volume owing to the void growth during plastic deformation is proposed based on the law of mass conservation, as follows:

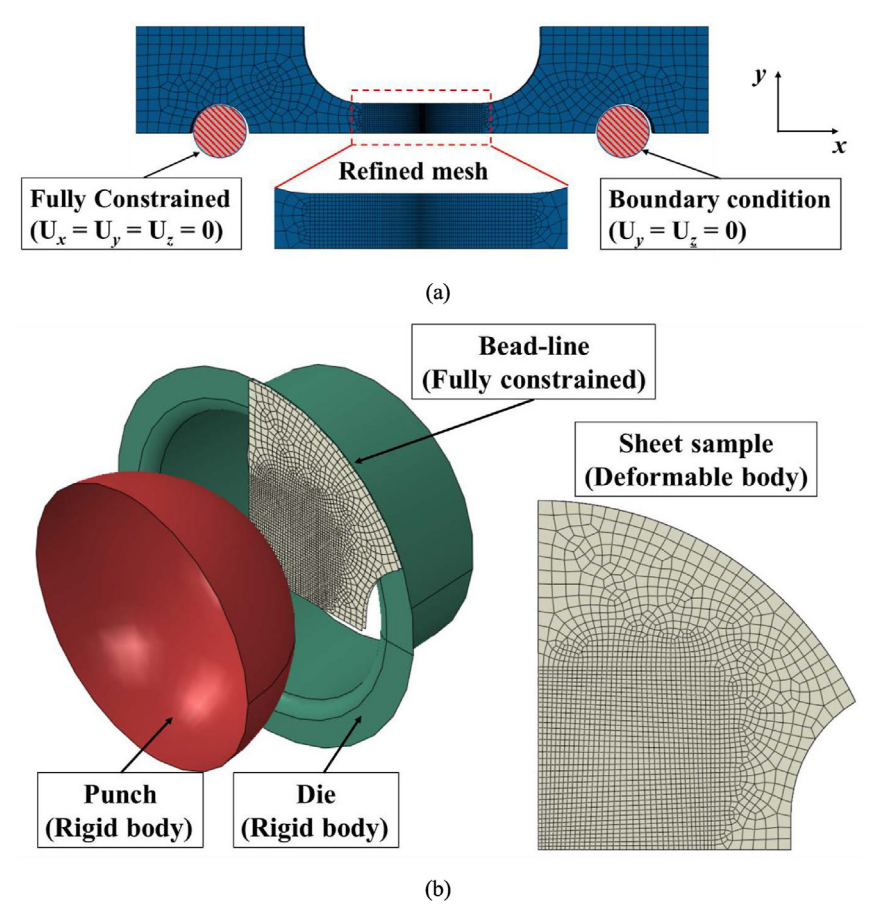


Fig. 5 – Finite element model with the prescribed boundary conditions used for the (a) hot uniaxial tension and (b) hot Nakajima tests [54,56].

$$df_{g} = (1 - f)d\varepsilon_{p} : I \tag{11}$$

where $d\varepsilon_p$ is a tensor of the plastic strain increment in the matrix, I is the second-order identity tensor, and the symbol ":" denotes the double dot product of the two tensors. As discussed in previous studies [37,38,67,68], the original evolution laws of the changes in void volume obtained from the GTN models could not capture the damage behaviors of metals at low triaxialities, such as under shear loading. In this study, the additional contribution of df_s proposed by Nahshon and Hutchinson [37] is considered, and the evolution law is as follows:

$$df_{s} = k_{w} \cdot f \cdot \omega(\sigma) \cdot \frac{s : d\epsilon_{p}}{\overline{\sigma}}$$
(12)

where k_w is the material constant, \mathbf{s} is the deviatoric stress tensor from the Cauchy stress $\mathbf{\sigma}$, and $\omega(\mathbf{\sigma})$ is the function of the Lode angle θ defined as

$$\omega(\sigma) = 1 - (\cos 3\theta)^2 \text{ and } \cos 3\theta = \frac{3\sqrt{3}J_3}{2J_2\sqrt{J_2}}$$
 (13)

where J_2 and J_3 are the second and third invariants of the deviatoric stress, respectively. Note that under uniaxial tension, the value of the Lode angle function $\omega(\sigma)$ is zero, and this value becomes unity and zero under plane strain and balanced biaxial tensions, respectively.

In addition, Nielsen and Tvergaard [40] proposed an improved model to reduce the strong influence of shear-induced failure under a high triaxiality condition as follows:

$$\omega_0 = \omega(\sigma) \cdot \Omega(T) \text{ with } \Omega(T) = \left\{ \begin{array}{ll} 1 & T < T_1 \\ (T - T_2)/(T_1 - T_2) \text{ for } T_1 \leq T < T_2 \\ 0 & T > T_2 \end{array} \right. \tag{14}$$

where T is the stress triaxiality and T_1 and T_2 are material coefficients. Subsequently, the evolution law of df_s is reformulated as follows:

$$df_{s} = k_{w} \cdot f \cdot \omega_{0} \cdot \frac{\mathbf{s} : d\varepsilon_{p}}{\overline{\sigma}}$$
(15)

The nucleation of the new voids is assumed to obey the strain-controlled nucleation rule and Gaussian distribution function as follows:

$$df_{n} = A \cdot (d\overline{\epsilon}_{m}) \tag{16}$$

$$A = \frac{f_N}{S_N \sqrt{2\pi}} e^{\left[-\frac{1}{2} \left(\frac{\bar{e}_{m-e_N}}{S_N}\right)^2\right]}$$
(17)

where $\bar{\epsilon}_m$ is the effective strain in the matrix, $d\bar{\epsilon}_m$ is the incremental form of the effective strain, f_N is the new volume fraction of the voids owing to nucleation, ϵ_N is the average

Table 2 — Finite element simulation conditions.							
Material property		Parameters used in the hot uniaxial tension tests					
Density 4.512 g/cm ³	Elastic modulus 110 GPa	Element type C3D8R	Average mesh size $1 \text{ mm} \times 1 \text{ mm}$	Refined mesh size $0.1 \text{ mm} \times 0.1 \text{ mm}$			
Parameters used in the hot Nakajima tests							
Element type C3D8R	Punching speed 0.5 mm/s	Friction coefficient 0.4	Average mesh size 1 mm $ imes$ 1 mm	Refined mesh size $0.5 \text{ mm} \times 0.5 \text{ mm}$			

value of the normal distribution of nucleation strain, and $S_{\rm N}$ is the standard deviation of the Gaussian distribution.

In this study, the nucleation of a new void is assumed to be linearly dependent on strain rates; therefore, the material constant f_N in Eq. (17) can be expressed as [28,69].

$$f_{N}(\dot{\varepsilon}) = l_{0} \cdot (\dot{\varepsilon} - \dot{\varepsilon}_{0}) + l_{1} \tag{18}$$

where l_0 and l_1 are material constants to be fitted using the experimental data. As mentioned in previous studies [28,69], the number of newly nucleated voids increase gradually as temperature and loading rates increase; therefore, the proposed assumption is fairly plausible.

Note that the model considered in this study is known as the "GTN-shear" model.

3.3. Finite element modeling

In this study, FE modeling was conducted using commercial FE software, namely, ABAQUS/Explicit (Dassault Systemes) [70]. The three-dimensional FE models of the specimen samples used in the hot uniaxial tension tests were generated using the element type C3D8R (solid element with an eightnode brick and reduced integration point). Fig. 5 (a) shows the FE model under monotonic loading at a high temperature. The average element size of the sheet sample was 1 mm \times 1 mm (length \times width), and a refined mesh with a mesh size of 0.1 mm \times 0.1 mm was used in the gauge length area. Five elements along the thickness direction were determined after mesh-size sensitivity tests [71]. As shown in the figure, half the specimen sample was used considering the symmetric condition, and this reduced computation time. The simulations were conducted under boundary conditions that were similar to those applied in the experiments. To compare the experimental and simulated results, the load and displacement in the gauge length area were extracted from the FE simulation results. Notably, when the failure condition obtained from the GTN-shear model satisfies the overall integration points in the FE model, the corresponding element is removed in the FE model.

Fig. 5 (b) describes the three-dimensional FE model used for the hot Nakajima tests. The model is composed of a punch, die, and sheet sample. To improve computational efficiency, all directions of the displacement and rotation of the outer edge of the sheet sample were constrained along the bead line instead of only by the holder system, which is denoted as the fixed assumption in the figure. Similar to the experiment, the punch moved to the sheet sample at a constant speed of 0.5 mm/s. To reduce computation time and increase accuracy, the tools were set as analytical rigid

bodies and only a quarter of a sheet sample was modeled. The average mesh size of the sheet sample with C3D8R was 1 mm \times 1 mm (length \times width), and a refined mesh with dimensions of 0.5 mm \times 0.5 mm was used in the contact area with the punch. Five elements along the thickness direction were determined after mesh-size sensitivity tests [72,73]. A friction coefficient of 0.4 was set between the sheet sample and the tools [74].

The simulated Ti–6Al–4V alloy sheets were assigned a density of 4.512 g/cm³, Young's modulus of 110 GPa, and Poisson's ratio of 0.33 to model linear isotropic elasticity. The FE simulation conditions are summarized in Table 2.

3.4. Numerical implementation

A stress-integration procedure was implemented on the proposed constitutive models by following the general backward-Euler return mapping algorithm [38,75] and executed using ABAQUS/Explicit via VUMAT [70]. For a total strain increment, $\Delta\epsilon$, the stress and evolutionary state variables should be updated at time $t+\Delta t$. The total strain increment is decomposed into two strain increments as

$$\Delta \varepsilon = \Delta \varepsilon_e + \Delta \varepsilon_p \tag{19}$$

where $\Delta \epsilon_e$ and $\Delta \epsilon_p$ represent the elastic and plastic strain increments, respectively.

For an isotropic elastic material, the relationship between the stress and strain tensors is given as

$$\Delta \sigma = \mathbf{C} : \Delta \varepsilon_{e} \tag{20}$$

$$\mathbf{C} = 2G\mathbf{I}_4 + \left(\mathbf{K} - \frac{2}{3}G\right)\mathbf{I} \bigotimes \mathbf{I} \tag{21}$$

where C is the linear isotropic elasticity tensor and G and K are the shear and bulk moduli, respectively. Additionally, I_4 and I are the fourth and second-order identity tensors, respectively.

According to the associated flow rule, the plastic strain increment is expressed as

$$\Delta \varepsilon_p = \Delta \lambda \frac{\partial \Phi}{\partial \sigma} = \Delta \lambda a \tag{22}$$

where Φ is defined in Eq. (7). Additionally, $\Delta\lambda$ and $\frac{\partial\Phi}{\partial\sigma}$ (= a) are the plastic multiplier and the flow direction tensor, respectively.

The numerical integration algorithm is based on a trial predictor stress σ^T (= σ + C: $\Delta\epsilon$), and subsequently, the new current stress state σ_c is updating when $\Phi(\sigma^T) > 0$ as follows:

$$\sigma_{c} = \sigma^{T} - \Delta \lambda C : a_{c}$$
 (23)

The initial estimate of a_c is equal to the normal direction under a trial predictor stress. To satisfy the consistency condition at the new current stress, further iterations are required. Residual tensor r is calculated as follows:

$$\mathbf{r} = \mathbf{\sigma} - \mathbf{\sigma}_{c} = \mathbf{\sigma} - (\mathbf{\sigma}^{T} - \Delta \lambda \mathbf{C} : \mathbf{a}_{c})$$
(24)

where σ is the backward Euler stress. Taylor's expansion is applied to the residual of Eq. (24) such that

$$r_{\textit{new}} = r_{\textit{old}} + d\sigma_{c} + (d\Delta\lambda)G : a_{c} + \Delta\lambda G : \frac{\partial a_{c}}{\partial \sigma} d\sigma_{c} \tag{25} \label{eq:25}$$

where $d\sigma_c$ is the incremental stress, $d\Delta\lambda$ is the change in the plastic multiplier, r_{old} is the residual stress from the previous step, and $\frac{\partial a_c}{\partial \sigma}$ is the second derivative of Φ . Assuming that the present residual is equal to zero, Eq. (25) provides

$$\begin{split} d\sigma_c &= -\left(I + \Delta\lambda C \colon\! \frac{\partial a_c}{\partial \sigma}\right)^{-1} \colon\! (r_{old} + (d\Delta\lambda)C \colon\! a_c) = -\,Q \colon\! r_{old} \\ &- (d\Delta\lambda)Q \colon\! C \colon\! a_c \end{split} \tag{26}$$

In addition, Taylor's expansion on the Gurson-type model, Φ , in Eq. (7) is expressed as

$$\Phi_{\textit{new}} = \Phi_{\textit{old}} + \frac{\partial \Phi}{\partial \sigma} d\sigma + \frac{\partial \Phi}{\partial f_*} \frac{\partial f_*}{\partial f} df + \frac{\partial \Phi}{\partial \sigma_{IH}} d\sigma_{IH}$$
 (27)

where

$$\frac{\partial \Phi}{\partial f_*} = 2q_1 \cosh\left(q_2 \frac{3p}{2\sigma_H}\right) - 2q_3 f_* \tag{28}$$

$$\frac{\partial f_*}{\partial f} = \begin{cases} 1\\ \frac{f_u - f_c}{f_f - f_c} & \text{if } f_c \le f \le f_c\\ 0 & f_f \le f \end{cases}$$
(29)

$$\frac{\partial \Phi}{\partial \sigma_{IH}} = -\frac{2(\overline{\sigma})^2}{(\sigma_{IH})^3} - \frac{3q_1q_2f_*p}{(\sigma_{IH})^2} sinh\left(q_2\frac{3p}{2\sigma_{IH}}\right) \tag{30}$$

$$df = \left[(1 - f) \boldsymbol{a}_c : I + k_w \cdot f \cdot \boldsymbol{\omega}_0 \cdot \frac{\boldsymbol{s}}{\overline{\sigma}} : \boldsymbol{a}_c + A \cdot \frac{\boldsymbol{\sigma} : \boldsymbol{a}_c}{(1 - f) \sigma_{IH}} \right] (d\Delta \lambda) \tag{31}$$

$$\begin{split} d\sigma_{IH} &= \frac{\partial \sigma_{IH}}{\partial \overline{\epsilon}} d\overline{\epsilon} + \frac{\partial \sigma_{IH}}{\partial \dot{\epsilon}} d\dot{\epsilon} = \left(\frac{\partial \sigma_{IH}}{\partial \overline{\epsilon}} + \frac{1}{\Delta t} \frac{\partial \sigma_{IH}}{\partial \dot{\epsilon}} \right) \frac{\sigma : a_c}{(1-f)\sigma_{IH}} d\Delta\lambda \\ &- \left(\frac{\partial \sigma_{IH}}{\partial \dot{\epsilon}} \right) \dot{\epsilon}_{old} \end{split} \tag{32}$$

In Eq. (32), Δt is the time increment and $\dot{\epsilon}_{old}$ is the strain rate from the previous step.

After setting the yield condition Φ_{new} to zero, the increment in the plastic multiplier is derived as

$$d\Delta\lambda = \frac{\Phi_{old} - Lh_1 \dot{\epsilon}_{old} - a_c : Q : r_{old}}{a_c : Q : a_c - \frac{\partial \Phi}{\partial f_c} \frac{\partial f_c}{\partial f} df - \frac{\partial \Phi}{\partial \sigma_{tot}} L\overline{h}}$$
(33)

where

$$L = \frac{\sigma : a_{c}}{(1 - f)_{\sigma_{1H}}}, h_{1} = \frac{\partial \sigma_{1H}}{\partial \dot{\epsilon}}, \overline{h} = \frac{\partial \sigma_{1H}}{\partial \overline{\epsilon}} + \frac{1}{\Delta t} \frac{\partial \sigma_{1H}}{\partial \dot{\epsilon}}$$
(34)

When the updated value of Φ is within a specified tolerance, e.g., 10^{-6} , the iteration is terminated.

4. Results and discussion

4.1. Fractographic observations

To identify the physical frame of the observed mechanical behaviors under high-temperature conditions, microscopic observations were supplemented. The fractographic images of the specimens were captured using an SEM. Fig. 6 shows the representative fractographic images along the rolling plane under uniaxial tension at a strain rate of 5×10^{-3} /s, including under uniaxial-stretch (W40), plane-strain (W75), and biaxial-stretch (W150) deformation modes, obtained from the hot Nakajima tests.

The fractographic images shown in Fig. 6 (a) and (d) reveal that the densities of the dimples on the fractured surfaces under uniaxial tension and the balanced-biaxial deformation mode is higher than those under uniaxial-stretch and planestrain deformation modes obtained from the hot Nakajima tests (refer to Fig. 6 (b) and (c)). The fractographic images obtained under uniaxial tension and the biaxial deformation modes show that the formation of round dimples is the main mechanism of failure; therefore, the significant plastic deformation during fracture can be explained. The plastic deformations at these loads increase the growth and coalescence of voids, and the corresponding dimples appear parallel to the loading direction [76]. In contrast, the fractographic images under the uniaxial-stretch and plane-strain deformation modes in Fig. 6 (b) and (c) show elongated dimples that are termed inter-void shearing dimples. More specifically, more inter-void shearing dimples are observed in the fractographic images of the uniaxial-stretch sample in comparison with those observed in the fractography of the planestrain deformation sample. Under these loading conditions, voids cannot sufficiently grow for coalescing; therefore, failure occurs owing to shear localization in the thickness direction [77]. These observations highlight the importance of the shearing effect in FE simulations; however, this effect was not considered in previous studies [54].

As discussed in the previous section, the original GTN model could capture the damage behaviors of metals owing to voids but could not predict the mechanical behaviors owing to inter-void shearing. The GTN model modified by Nahshon and Hutchinson [37] described the damage behavior owing to the inter-void shearing effect; however, the model has a limitation, i.e., the material damage owing to shearing evolves rapidly even under high triaxiality. The proposed GTN-shear model could determine the effect of inter-void shearing on damage evolution with respect to the loading path, as observed from the fractographic images obtained after the hot Nakajima tests. The corresponding results will be discussed later.

4.2. Monotonic loading at a high temperature

The material constants related to strain hardening and the original GTN damage models were identified by applying uniaxial tension at various strain rates, as reported in the authors' previous study [54]; these constants are listed in Table 3. Notably, the stress triaxiality of uniaxial tension,

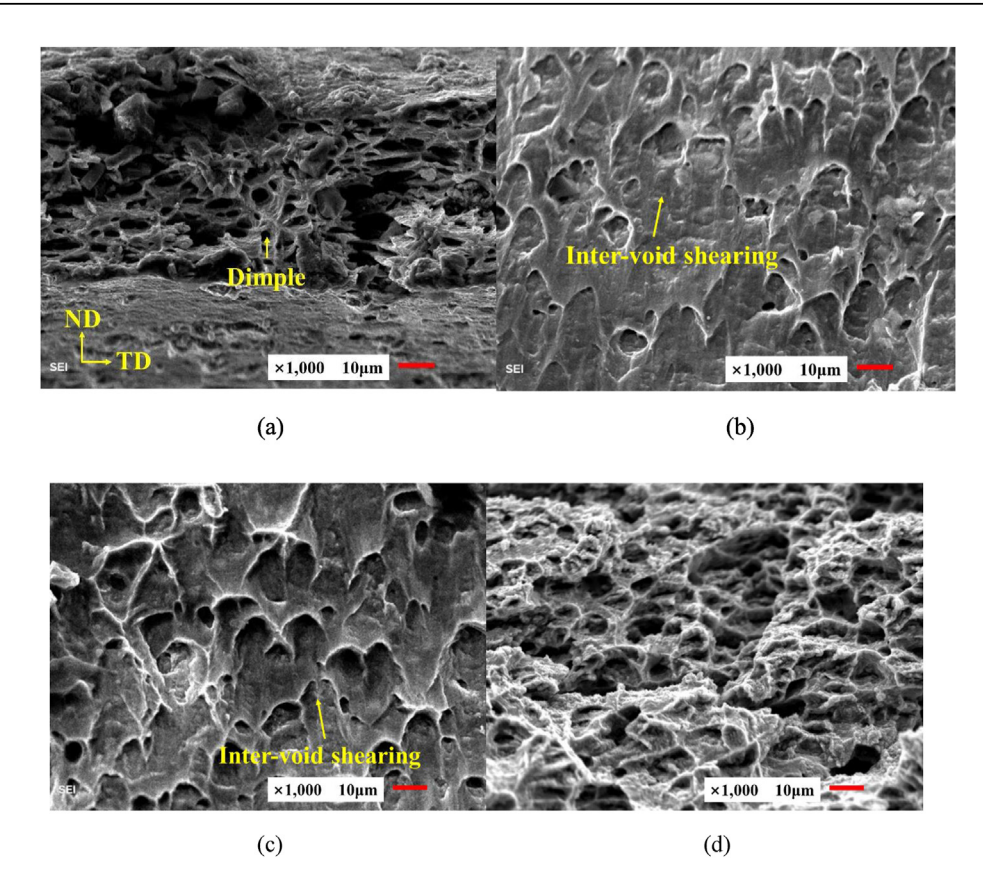


Fig. 6 – Fractographic images (1000 \times) owing to (a) the hot uniaxial tension tests at a strain rate of 5 \times 10⁻³/s and those obtained from the (b) uniaxial-stretch (W40), (c) plane-strain (W75), and (d) biaxial-stretch (W150) deformation modes under the hot Nakajima tests at 650 °C [54].

corresponding to $T=\frac{1}{3}$, does not affect the damage evolution owing to inter-void shearing in the GTN-shear model. Therefore, the corresponding parameters related to the evolution of shear damage, as per Eqs. (14) and (15), can be calibrated using the experimental data obtained from the hot Nakajima tests in the next section.

Fig. 7 shows the comparison between the engineering stress-strain curves obtained from experimental and

numerical results under uniaxial tension, three different strain rates, and a high temperature. The simulated and experimental results obtained under uniaxial tension and a high temperature at strain rates of 5 \times 10 $^{-4}$ /s and 5 \times 10 $^{-2}$ /s were in good agreement in terms of maximum stress and fracture strain. The simulated results under uniaxial tension and a high temperature at a strain rate of 5 \times 10 $^{-3}$ /s showed small discrepancies in relation to the corresponding

Table 3 $-$ Material constants used in the proposed constitutive models.							
Voce hardening	Strain-rate sensitivity expressed in Eq. (3)						
Α	В		С		m		
130.32	97.8	97.83			0.2089		
Softening law expressed in Eq. (4)–(5)							
q		r		p_0	p_1		
15		1.9		3.03	0.8		
Original GTN model expressed in Eq. (8), (12), (17), and (20)							
$f_{\rm c}$	f_f	$\epsilon_{ m N}$	S_N	l_0	l_1		
0.10	0.13	0.45	0.1	1.364	0.0075		
GTN-shear model expressed in Eq. (14)							
k _w			T ₁		T ₂		
26.8		0.0 0.6					

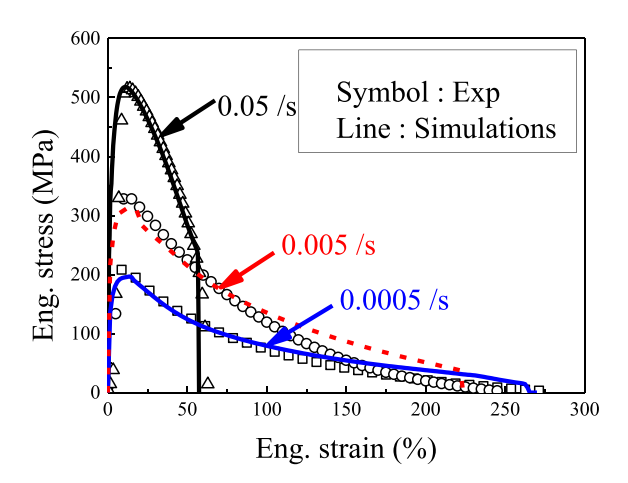


Fig. 7 — Comparison between the engineering stress—strain curves obtained from the experimental and simulated results from the GTN-shear model at various strain rates under uniaxial tension at 650 °C. The experimental data at strain rates of 5 \times 10⁻⁴/s and 5 \times 10⁻²/s were obtained from Ref. [54].

experimental results after 100% engineering strain; however, the predicted ultimate tensile strength was in good agreement with the experimental data.

Fig. 8 (a) and (b) show the experimental sample used for the hot uniaxial tension tests at a strain rate of 5×10^{-3} /s and the corresponding von-Mises stress contour at the onset of fracture obtained from the FE simulations, respectively. The simulations and the experiments yielded remarkably elongated samples, and the simulated sample correlated reasonably well with the samples used in the experiments. This suggests that the strain-hardening behaviors, including the strain-rate sensitivity and the flow-softening and damage behaviors, should be explicitly addressed in the FE

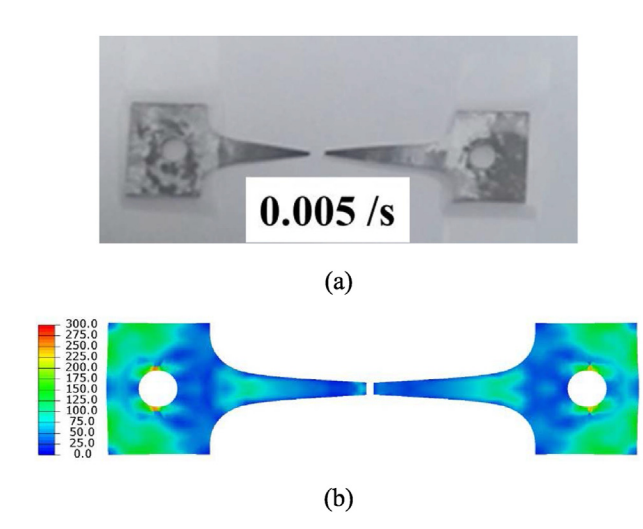


Fig. 8 – (a) Photograph of the fractured sample under uniaxial tension and a high temperature and the (b) corresponding simulation results showing the von-Mises stress (unit: MPa) at a strain rate of 5 \times 10⁻³/s.

simulations to obtain an accurate prediction of the stress-strain curves.

Fig. 9 (a) and (b) show the distribution of the total volume fraction of voids defined in Eq. (10) and the Lode angle function $\omega(\sigma)$ associated with the evolution of the void volume owing to inter-void shearing. As shown in the figures, the void volume fraction evolves in the middle of the sheet samples, and the void evolution owing to shearing is negligible because the Lode angle function is nearly zero in the corresponding region.

4.3. Multiaxial loading in the hot Nakajima tests

The proposed material models were incorporated into the FE simulation models for conducting the hot Nakajima tests under multiaxial loading conditions. The predicted punch force-stroke relationships obtained from the GTN-shear model were compared with the corresponding experimental data, as shown in Fig. 10. The samples with different widths in the punch-contacted region, i.e., W40, W75, and W150, are observed to experience the uniaxial-stretch, plane-strain, and biaxial-stretch deformation modes, respectively.

All the predicted curves for various width conditions were in good agreement with the corresponding experimental data, as presented in Fig. 10. In particular, the simulated curves obtained from the W40 sample were in good agreement with the experimentally obtained curves with reasonable accuracy. This confirms the suitability of the adopted strain-hardening model, which includes strain-rate sensitivity and the flow stress softening effect, under a wide strain range. The proposed GTN-shear model could capture the maximum load and punch stroke and reproduce the experimentally measured punch stroke at failure with a marginal error regardless of the sample dimensions.

Furthermore, the predicted displacements at the onset of failure obtained from the proposed GTN-shear model and the original GTN model under various width conditions were compared, as shown in Fig. 11. The original GTN model was found to reproduce the punch load—stroke curves; however, some deviations were noted from the corresponding experimental results in the predicted stroke at failure under certain

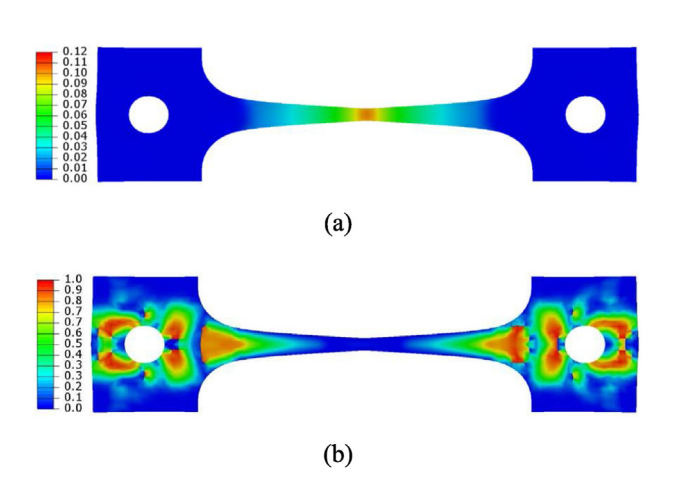


Fig. 9 – (a) Distribution of the total volume fraction of voids and the (b) Lode angle function $\omega(\sigma)$ before fracture defined in Eq. (13) obtained from the FE simulations.

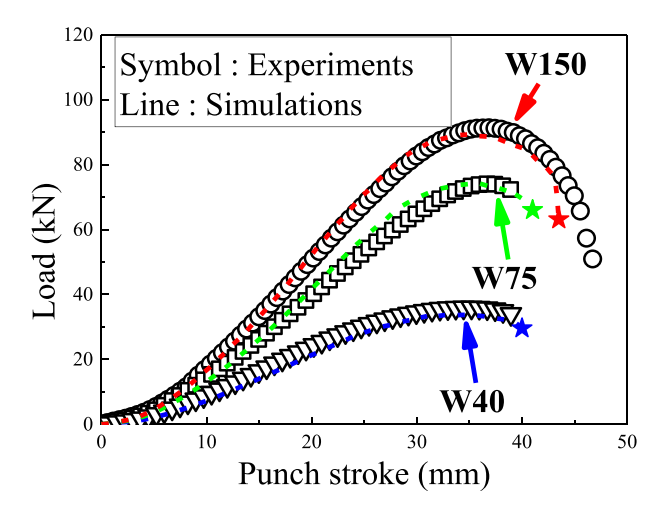


Fig. 10 — Punch load—stroke plots obtained from the simulated (dot lines) and experimental (symbol) multiaxial loading tests using the GTN-shear model. The star symbol represents the failure point of the material.

width conditions. As illustrated in Fig. 11, the original GTN model overestimated the punch stroke at failure for the W40 and W75 samples, and the GTN-shear model yielded better predictions than those obtained from the original GTN model. Additionally, minor differences were observed between the predicted results from the original GTN and GTN-shear models for the W150 samples.

The strokes predicted at the onset of failure were analyzed using the same approach as the fractographic analysis. The original GTN model assumed that the material fails due to void growth and coalescence under a given hydrostatic pressure. Fractography of the W150 samples showed numerous large dimples in the matrix, which validates the assumption under the original GTN model. However, different types of failure, e.g., that owing to inter-void shearing, were observed in the fractographic images of the W40 and W75 samples. These failures were inapplicable to the original GTN model for predicting the deformation behavior of the samples under high-temperature conditions. Therefore, the results

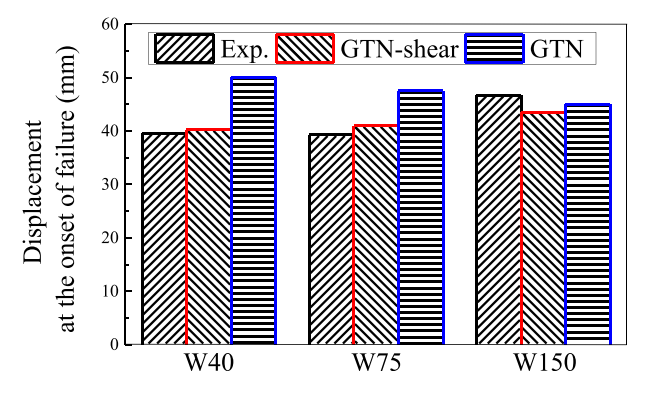


Fig. 11 – Comparison between the experimental and numerical displacements at the onset of failure. The predicted displacements from the original GTN model were obtained from Ref. [54].

indicated the requirement of an improved damage model for predicting the hot deformation behavior of Ti-6Al-4V alloy sheets.

The evolution of the total volume fractions of the voids in samples W40 and W75 during the hot Nakajima tests is shown in Fig. 12, and the predicted results obtained from the GTN-shear model are compared with those obtained from the original GTN model. As shown in the figure, the inter-void shearing effect was clearly observed in the evolution of the total volume fraction of the voids. After a punching stroke of 30 mm, the total volume fraction of the voids obtained from the FE simulations using the GTN-shear model rapidly increased and approached the volume fraction of the voids at the onset of material failure. In contrast, the original GTN model yielded a relatively slow evolution of the total volume fraction of voids. Therefore, discrepancies were noted between the simulation and experimental punch strokes at material failure.

Fig. 13 (a)-(c) show the predicted contours of state variables obtained using the GTN-shear model and the W40 sample at the onset of material failure. The equivalent plasticstrain distribution shown in Fig. 13 (a) reveals a small plastic deformation at the pole of the sample. Fig. 13 (b) displays the contour of the Lode angle function $\omega(\sigma)$ of the W40 sample and reveals that the drawing deformation modes in the overall locations are between the uniaxial-stretch and plane-strain deformation modes. The uniaxial stretch mode, which is equivalent to $\omega(\sigma) = 0.0$, is observed at the pole of the W40 sample. The drawing deformation mode, which is equivalent to $\omega(\sigma)$ < 1.0, is predicted to be located over the remaining sample area. Fig. 13 (c) reveals a high volume fraction of voids owing to the inter-void shearing effect between the pole of the sample and the clamping area, and the fracture location of the W40 samples is affected by inter-void shearing, as shown in Fig. 13 (d).

Fig. 14 (a)—(c) present the simulated distribution of the equivalent strain, Lode angle function, and volume fraction of the voids under inter-void shearing, respectively, obtained using the W75 sample. Similar to the results obtained using

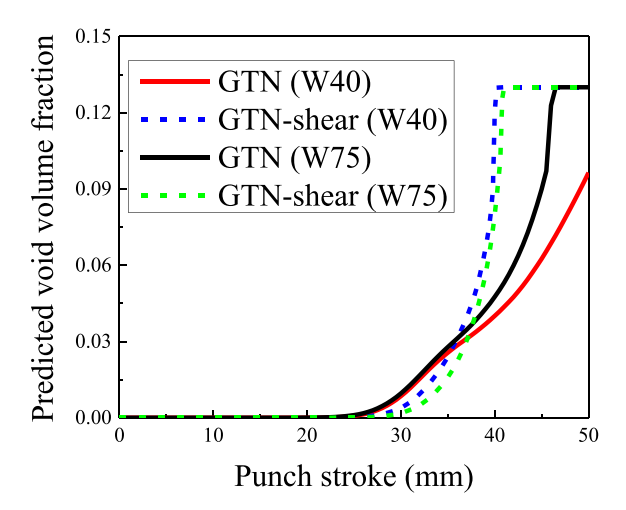


Fig. 12 — Comparison between the predicted volume fractions of the voids in samples W40 and W75 obtained using the original GTN and GTN-shear models.

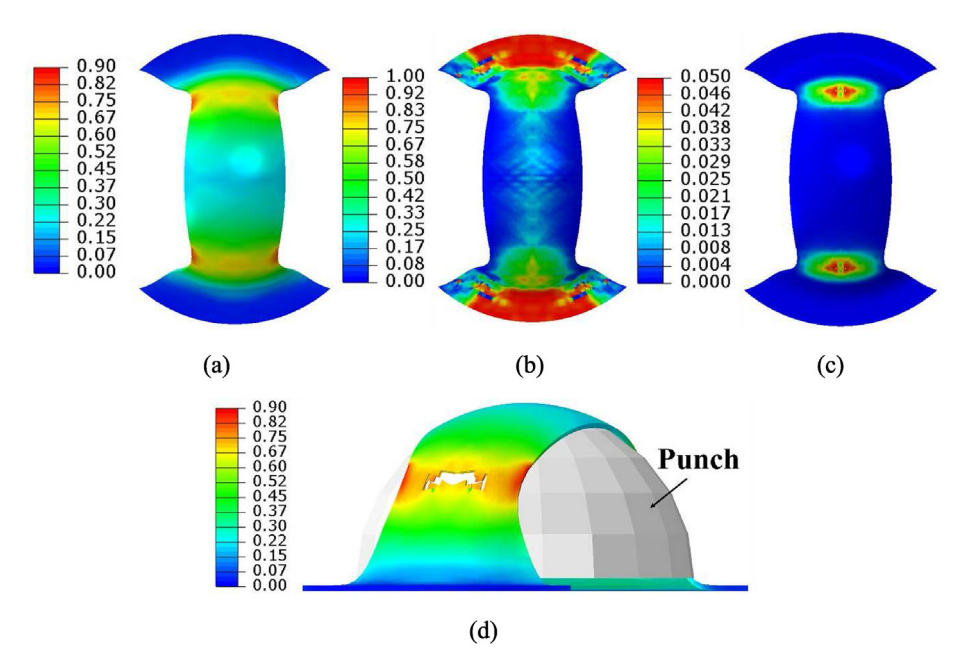


Fig. 13 — FE simulation results obtained using the GTN-shear model and the W40 sample: contour plots of (a) plastic strain, (b) Lode angle function $\omega(\sigma)$ defined in Eq. (13), (c) volume fraction of voids owing to inter-void shearing, and (d) fractured side view and its plastic-strain distribution.

the W40 sample, a small equivalent plastic strain is predicted at the pole of the W75 sample, as shown in Fig. 14 (a). The plane-strain stretch deformation mode is observed in Fig. 14 (b) when the value of the Lode angle function is unity. The volume fraction of voids under inter-void shearing presented in Fig. 14 (c) is predicted to be a maximum of 3%. Fig. 14 (d) reveals that the fracture location in the sample is associated with the location of the maximum volume fraction of voids owing to the inter-void shearing effect.

Notably, the Nahshon–Hutchinson model strongly influences the shear-induced damage evolution under the plane-strain deformation mode. The additional inter-void shearing model, which is expressed in Eq. (12), proposed by Nahshon and Hutchinson cannot reproduce the hot deformation behavior of Ti–6Al–4V alloy sheets because the experimental observations from the hot Nakajima tests reveal a small effect of inter-void shearing on the failure evolution in the plane-strain deformation mode. Therefore, the modified

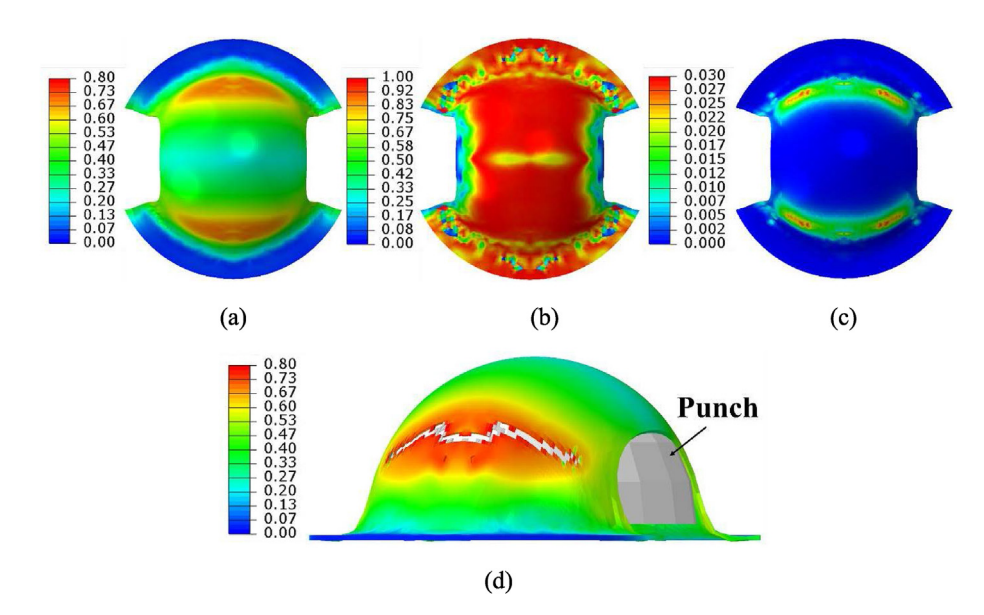


Fig. 14 — FE simulation results obtained from the GTN-shear model and the W75 samples: contour plots of (a) plastic strain, (b) Lode angle function $\omega(\sigma)$ defined in Eq. (13), (c) volume fraction of voids owing to inter-void shearing, and (d) fractured side view and its plastic-strain distribution.

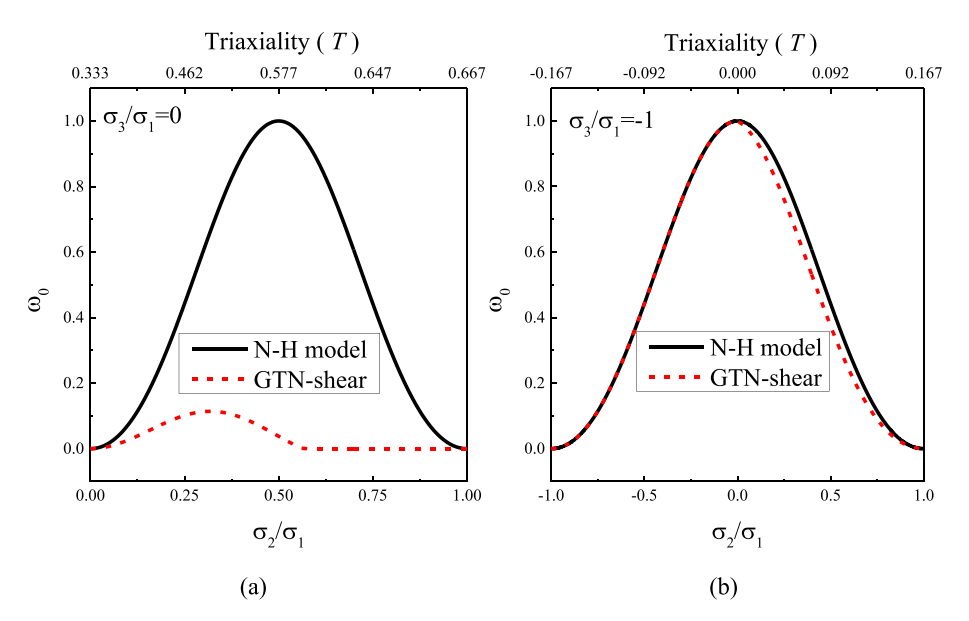


Fig. 15 – Comparison between the function $\omega_0 = \omega(\sigma) \bullet \Omega(T)$ defined in Eq. (14) with respect to the stress ratio σ_2/σ_1 and the corresponding stress triaxiality T under (a) plane-stress tension ($\sigma_3/\sigma_1 = 0$ and $\sigma_1 > 0$) and (b) shear-stress states applied under transverse stress ($\sigma_3/\sigma_1 = -1$ and $\sigma_1 > 0$). Note that the N–H model represents the Nahshon–Hutchinson model.

inter-void shearing model, which is expressed in Eq. (15), developed by Nielsen and Tvergaard [40] is suitable for describing the mechanical behavior at high temperatures under multi-axial loadings.

Fig. 15 (a) and (b) compare the values of the Lode angle function for the stress ratios and triaxialities obtained from the two material models under plane-stress tension and shear stress combined with transverse stress, respectively. As shown in Fig. 15 (a), the Nahshon-Hutchinson model introduces a large inter-void shearing effect under plane-strain tension. As displayed in the figure, the GTN-shear model introduces the interpolated function $\Omega(T)$ and reduces the additional inter-void shearing effect under plane-strain tension; however, the inter-void shearing effect remains under various stress states. As presented in Fig. 15 (b), small deviations are observed in the Lode angle functions obtained from the Nahshon-Hutchinson and GTN-shear models. Notably, the present study focuses on hot deformation behavior under plane-stress conditions; however, rigorous investigations are required under general stress states and will be presented in a complementary paper.

5. Summary and conclusions

In this study, the ductile damage fracture behavior of Ti-6Al-4V alloy sheets under high-temperature conditions was investigated via hot uniaxial tension and hot Nakajima tests. Corresponding FE simulations were performed using an improved Gurson-type model, namely, the GTN-shear model. The major findings of the present study are as follows.

- The GTN-shear model characterized the tensile behavior of the sheets under high temperatures, capturing the maximum stress and the ductility from the corresponding FE simulations. The FE simulations of the tensile tests under high-temperature conditions revealed that the intervoid shearing effect is negligible during these tests because the Lode angle function is almost zero.
- Several dimples of various sizes were observed in the fractographic images obtained from the hot tensile tests and the balanced biaxial-stretch deformation modes under the hot Nakajima tests, showing the classical ductile failure mechanism. In contrast, elongated dimples were observed under uniaxial-stretch and plane-strain deformation modes during the hot Nakajima tests, thereby revealing the inter-void shearing effect.
- The GTN-shear model captured the hot deformation behavior obtained from the hot Nakajima and hot uniaxial tensile tests. The experimental stress—strain (as well as load —displacement) curves and the displacements at the onset of material failure were in good agreement with the corresponding results obtained from the proposed model. An additional interpolated function $\Omega(T)$ included in the proposed GTN-shear model effectively controlled the intervoid shearing effect in the Ti-6Al-4V alloy sheets during hot Nakajima tests, promoting fracture at moderate levels of stress triaxiality.

Overall, the GTN-shear model based on micromechanics accounted for the complex hot deformation behavior of the Ti-6Al-4V alloy sheets, thereby accurately predicting the load histories and material failure positions under plane-stress

conditions. Future research will focus on validating the material model in terms of hot deformation behavior under general stress states.

Declaration of competing interest

The authors declare that they have no known competing financial interests or personal relationships that could have appeared to influence the work reported in this paper.

Acknowledgment

J. Ha appreciates the support of the New Hampshire Center for Multiscale Modeling and Manufacturing of Biomaterials (NH BioMade) project provided by the US National Science Foundation (NSF) EPSCoR award (#1757371). H. J. Bong appreciates the supports by the Fundamental Research Program of the Korea Institute of Materials Science (KIMS, PNK9460). Finally, this result was supported by "Regional Innovation Strategy (RIS)" through the National Research Foundation of Korea (NRF) funded by the Ministry of Education (MOE) (2021RIS-003).

REFERENCES

- Beal JD, Boyer R, Sanders D. Forming of titanium and titanium alloys. ASM Handb 2006;14B:656-70. ASM International.
- [2] Khan AS, Kazmi R, Farrokh B, Zupan M. Effect of oxygen content and microstructure on the thermomechanical response of three Ti-6Al-4V alloys: experiments and modeling over a wide range of strain-rates and temperatures. Int J Plast 2007;23:1105-25.
- [3] Kopec M, Wang K, Politis DJ, Wang Y, Wang L, Lin J. Formability and microstructure evolution mechanisms of Ti6Al4V alloy during a novel hot stamping process. Mater Sci Eng A 2018;719:72–81.
- [4] Sirvin Q, Velay V, Bonnaire R, Penazzi L. Mechanical behaviour modelling and finite element simulation of simple part of Ti-6Al-4V sheet under hot/warm stamping conditions. J Manuf Process 2019;38:472–82.
- [5] Souza PM, Mendiguren J, Chao Q, Beladi H, Hodgson PD, Rolfe B. A microstructural based constitutive approach for simulating hot deformation of Ti6Al4V alloy in the $\alpha+\beta$ phase region. Mater Sci Eng A 2019;748:30–7.
- [6] Khan AS, Suh YS, Kazmi R. Quasi-static and dynamic loading responses and constitutive modeling of titanium alloys. Int J Plast 2004;20:2233–48.
- [7] Carson C. Heat treating of titanium and titanium alloys. Heat Treat Nonferrous Alloy 2016;4E:0.
- [8] Gaddam R, Sefer B, Pederson R, Antti M-L. Study of alphacase depth in Ti-6Al-2Sn-4Zr-2Mo and Ti-6Al-4V. IOP Conf Ser Mater Sci Eng 2013;48:12002.
- [9] Gaddam R, Sefer B, Pederson R, Antti M-L. Oxidation and alpha-case formation in Ti-6Al-2Sn-4Zr-2Mo alloy. Mater Charact 2015;99:166-74.
- [10] Brice DA, Samimi P, Ghamarian I, Liu Y, Brice RM, Reidy RF, et al. Oxidation behavior and microstructural decomposition

- of Ti-6Al-4V and Ti-6Al-4V-1B sheet. Corros Sci 2016;112:338-46.
- [11] Velay V, Matsumoto H, Vidal V, Chiba A. Behavior modeling and microstructural evolutions of Ti-6Al-4V alloy under hot forming conditions. Int J Mech Sci 2016;108–109:1–13.
- [12] Alabort E, Putman D, Reed RC. Superplasticity in Ti-6Al-4V: characterisation, modelling and applications. Acta Mater 2015;95:428–42.
- [13] Alabort E, Barba D, Shagiev MR, Murzinova MA, Galeyev RM, Valiakhmetov OR, et al. Alloy-by-desing: application to titanium alloys for optimal superplasticity. Acta Mater 2019;178:275–87.
- [14] Bai Q, Lin J, Dean TA, Balint DS, Gao T, Zhang Z. Modelling od dominant softening mechanisms for Ti-6Al-4V in steady state hot forming conditions. Mater Sci Eng A 2013;559:352-8.
- [15] Chen SF, Li DY, Zhang SH, Han HN, Lee HW, Lee MG. Modelling continuous dynamic recrystallization of aluminum alloys based on the polycrystal plasticity approach. Int J Plast 2020;131:102710.
- [16] Odenberger E-L, Hertzman J, Thilderkvist P, Merklein M, Kuppert A, Stöhr T, et al. Thermo-mechanical sheet metal forming of aero engine components in Ti-6Al-4V – part 1: material characterisation. Int J Material Form 2013;6:391–402.
- [17] Paghandeh M, Zarei-Hanzaki A, Abedi HR, Vahidshad Y, Minarik P. The correlation of c-to-a axial ratio and slip activity of martensite including microstructures during thermomechanical processing of Ti-6Al-4V alloy. J Mater Res Technol 2022;18:577-83.
- [18] Paghandeh M, Zarei-Hanzaki A, Abedi HR, Vahidshad Y. On the warm temperature strain accommodation mechanisms of Ti-6Al-4V alloy holding different starting microstructures. J Mater Res Technol 2021;14:496–506.
- [19] Paghandeh M, Zarei-Hanzaki A, Abedi HR, Vahidshad Y. The enhanced warm temperature ductility of Ti-6Al-4V alloy through strain induced martensite reversion and recrystallization. Mater Lett 2021;302:130405.
- [20] Paghandeh M, Zarei-Hanzaki A, Abedi HR, Vahidshad Y, Kawałko J, Dietrich D, et al. Compressive/tensile deformation behavior and the correlated microstructure evolution of Ti-6Al-4V titanium alloy at warm temperatures. J Mater Res Technol 2021;10:1291-300.
- [21] Vanderhasten M, Rabet L, Verlinden B. Deformation mechanisms of Ti-6Al-4V during tensile behavior at low strain rate. J Mater Eng Perform 2007;16:208–12.
- [22] Leclerc J, Nguyen V-D, Pardoen T, Noels L. A micromechanics-based non-local damage to crack transition framework for porous elastoplastic solids. Int J Plast 2020;127.
- [23] Chen D, Li Y, Yang X, Jiang W, Guan L. Efficient parameters identification of a modified GTN model of ductile fracture using machine learning. Eng Fract Mech 2021;245.
- [24] Woelke PB. Simplification of the Gurson model for large-scale plane stress problems. Int J Plast 2020;125:331–47.
- [25] Gurson AL. Continuum theory of ductile rupture by void nucleation and growth. Part I: yield criteria and flow rules for porous ductile media. ASME J Eng Mater Technol 1977;99:2–15.
- [26] Tvergaard V, Needleman A. Analysis of the cup-cone fracture in a round tensile bar. Acta Metall 1984;32:157–69.
- [27] Bergo S, Morin D, Børvik T, Hopperstad OS. Micromechanics-based identification of a ductile fracture model for three structural steels. Eng Fract Mech 2020;224.
- [28] Gao T, Ying L, Hu P, Han X, Rong H, Wu Y, et al. Investigation on mechanical behavior and plastic damage of AA7075

- aluminum alloy by thermal small punch test: experimental trials, numerical analysis. J Manuf Process 2020;50:1–16.
- [29] Gholipour H, Biglari FR, Nikbin K. Experimental and numerical investigation of ductile fracture using GTN damage model on in-situ tensile tests. Int J Mech Sci 2019;164:105170.
- [30] Chiyatan T, Uthaisangsuk V. Mechanical and fracture behavior of high strength steels under high strain rate deformation: experiments and modelling. Mater Sci Eng A 2020;779:139125.
- [31] Ali AN, Huang S-J. Ductile fracture behavior of ECAP deformed AZ61 magnesium alloy based on response surface methodology and finite element simulation. Mater Sci Eng A 2019;746:197–210.
- [32] Yang S, Ling X, Xue L. Application of small punch test to investigate mechanical behaviours and deformation characteristics of Incoloy800H. J Alloys Compd 2018;765:497–504.
- [33] Allahverdizadeh N, Gilioli A, Manes A, Giglio M. An experimental and numerical study for the damage characterization of a Ti-6AL-4V titanium alloy. Int J Mech Sci 2015;93:32-47.
- [34] Tang B, Wu F, Wang Q, Liu J, Guo N, Ge H, et al. Damage prediction of hot stamped boron steel 22MnB5 with a microscopic motivated ductile fracture criterion: experiment and simulation. Int J Mech Sci 2020;169.
- [35] Nasir MW, Chalal H, Abed-Meraim F. Formability prediction using bifurcation criteria and GTN damage model. Int J Mech Sci 2021;191:106083.
- [36] He Z, Zhu H, Hu Y. An improved shear modified GTN model for ductile fracture of aluminium alloys under different stress states and its parameters identification. Int J Mech Sci 2021;192:106081.
- [37] Nahshon K, Hutchinson JW. Modification of the Gurson model for shear failure. Eur J Mech Solid 2008;27:1–17.
- [38] Nahshon K, Xue Z. A modified Gurson model and its application to punch-out experiments. Eng Fract Mech 2009;76:997—1009.
- [39] Xue L. Constitutive modeling of void shearing effect in ductile fracture of porous materials. Eng Fract Mech 2008;75:3343—66.
- [40] Nielsen KL, Tvergaard V. Ductile shear failure or plug failure of spot welds modelled by modified Gruson model. Eng Fract Mech 2010;77:1031–47.
- [41] Li WT, Cai ZY, Li H, Peng LF, Lai XM, Fu MW. The modified GTN-Thomason criterion for modelling of ductile fracture considering shear factor and size effect in micro-scaled plastic deformation. Int J Mech Sci 2021;204:106540.
- [42] Madou K, Leblond J-B. A Gurson-type criterion for porous ductile solids containing arbitrary ellipsoidal voids—II: determination of yield criterion parameters. J Mech Phys Solid 2012;60:1037—58.
- [43] Madou K, Leblond J-B, Morin L. Numerical studies of porous ductile materials containing arbitrary ellipsoidal voids — II: evolution of the length and orientation of the void axes. Eur J Mech Solid 2013;42:490–507.
- [44] Gologanu M, Leblond J-B, Devaux J. Approximate models for ductile metals containing non-spherical voids—case of axisymmetric prolate ellipsoidal cavities. J Mech Phys Solid 1993;41:1723—54.
- [45] Castañeda PP, Zaidman M. Constitutive models for porous materials with evolving microstructure. J Mech Phys Solid 1994:42:1459—97.
- [46] Aravas N, Ponte Castañeda P. Numerical methods for porous metals with deformation-induced anisotropy. Comput Methods Appl Mech Eng 2004;193:3767—805.

- [47] Danas K, Ponte Castañeda P. A finite-strain model for anisotropic viscoplastic porous media: II – applications. Eur J Mech Solid 2009;28:387–401.
- [48] Danas K, Ponte Castañeda P. A finite-strain model for anisotropic viscoplastic porous media: I theory. Eur J Mech Solid 2009;28:387—401.
- [49] Habibi N, Zarei-Hanzaki A, Abedi H-R. An investigation into the fracture mechanisms of twinning-induced-plasticity steel sheets under various strain paths. J Mater Process Technol 2015;224:102–16.
- [50] Katani S, Madadi F, Atapour M, Ziaei Rad S. Micromechanical modelling of damage behaviour of Ti-6Al-4V. Mater Des 2013;49:1016-21.
- [51] Valoppi B, Bruschi S, Ghiotti A, Shivpuri R. Johnson-Cook based criterion incorporating stress triaxiality and deviatoric effect for predicting elevated temperature ductility of titanium alloy sheets. Int J Mech Sci 2017;123:94–105.
- [52] Gao PF, Guo J, Zhan M, Lei ZN, Fu MW. Microstructure and damage based constitutive modelling of hot deformation of titanium alloys. J Alloys Compd 2020;831:154851.
- [53] Li J, Wang B, Huang H, Fang S, Chen P, Zhao J, et al. Behaviour and constitutive modelling of ductile damage of Ti-6Al-1.5Cr-2.5Mo-0.5Fe-0.3Si alloy under hot tensile deformation. J Alloys Compd 2019;780:284—92.
- [54] Bong HJ, Kim D, Kwon YN, Lee J. Predicting hot deformation behaviors under multiaxial loading using the Gurson-Tvergaard-Needleman damage model for Ti-6Al-4V alloy sheets. Eur J Mech Solid 2021;87:104227. https://doi.org/ 10.1016/j.euromechsol.2021.104227.
- [55] Jeong D, Kwon Y, Goto M, Kim S. Effect of superplastic forming exposure on fatigue crack propagation behavior of Ti-6Al-4V alloy. Met Mater Int 2016;22:747-54. https:// doi.org/10.1007/s12540-016-6075-9.
- [56] Bong HJ, Yoo D, Kim D, Kwon Y-N, Lee J. Correlative study on plastic response and formability of Ti-6Al-4V sheets under hot forming conditions. J Manuf Process 2020;58:775–86.
- [57] ASTM E21. Standard test methods for elevated temperature tension tests of metallic materials. 2020.
- [58] ISO 12004-2 (2021) Metallic materials determination of forming-limit curves for sheet and strip — Part 2: determination of forming-limit curves in the laboratory. second ed. International Organization for Standardization; 2021.
- [59] Murr LE, Staudhammer KP, Hecker SS. Effects of strain state and strain rate on deformation-induced transformation in 304 stainless steel: Part II. Microstructural study. Metall Trans A 1982;13:627–35. https://doi.org/ 10.1007/BF02644428.
- [60] Hedayati N, Hashemi R. Some practical aspects of digital image correlation technique to evaluate anisotropy coefficient and its comparison with traditional method. J Test Eval 2020;48:20180227. https://doi.org/10.1520/ JTE20180227.
- [61] Mousavi F, Hashemi R, Madoliat R. Measurement of directional anisotropy coefficients for AA7020-T6 tubes and prediction of forming limit curve. Int J Adv Manuf Technol 2018. https://doi.org/10.1007/s00170-018-1645-2.
- [62] Sung JH, Kim JH, Wagoner RH. A plastic constitutive equation incorporating strain, strain-rate, and temperature. Int J Plast 2010;26:1746–71.
- [63] Lee J, Kim JH, Lee MG, Barlat F, Zhou C, Chen Z, et al. Properties controlling the bend-assisted fracture of AHSS. Int J Plast 2015;75:100–20.
- [64] Seok D-Y, Kim D, Kim S-W, Bak J, Lee Y-S, Chung K. Fracture criterion for AZ31 Mg alloy plate at elevated temperature. Met Mater Int 2015;21:54—71.
- [65] Koh Y, Kim D, Seok D-Y, Bak J, Kim S-W, Lee Y-S, et al. Characterization of mechanical property of magnesium

- AZ31 alloy sheets for warm temperature forming. Int J Mech Sci 2015;93:204–17.
- [66] Quan G, Luo G, Liang J, Wu D, Mao A, Liu Q. Modelling for the dynamic recrystallization evolution of Ti-6Al-4V alloy in two-phase temperature range and a wide strain rate range. Comput Mater Sci 2015;97:136-47.
- [67] Xue L, Wierzbicki T. Ductile fracture initiation and propagation modeling using damage plasticity theory. Eng Fract Mech 2008;75:3276–93.
- [68] Davaze V, Vallino N, Feld-Payet S, Langrand B, Besson J. Plastic and fracture behavior of a dual phase steel sheet under quasi-static and dynamic loadings. Eng Fract Mech 2020;235:107165.
- [69] Ying L, Gao T, Rong H, Han X, Hu P, Hou W. On the thermal forming limit diagram (TFLD) with GTN mesoscopic damage model for AA7075 aluminum alloy: numerical and experimental investigation. J Alloys Compd 2019;802:675—93.
- [70] Abaqus. User's manual. USA.: Hibbit, Karlsson & Sorensen Inc; 2021. 2021.
- [71] Sánchez PJ, Huespe AE, Oliver J. On some topics for the numerical simulation of ductile fracture. Int J Plast

- 2008;24:1008-38. https://doi.org/10.1016/j.ijplas.2007.08.004.
- [72] Chalal H, Abed-Meraim F. Numerical predictions of the occurrence of necking in deep drawing processes. Metals 2017;7:455. https://doi.org/10.3390/ met7110455.
- [73] Dunand M, Mohr D. Hybrid experimental numerical analysis of basic ductile fracture experiments for sheet metals. Int J Solid Struct 2010;47:1130—43.
- [74] Bok H-H, Choi J, Barlat F, Suh DW, Lee M-G. Thermomechanical-metallurgical modeling for hot-press forming in consideration of the prior austenite deformation effect. Int J Plast 2014;58:154–83.
- [75] Simo JC, Hughes TJR. Computational inelasticity. Springer-Verlag; 1998.
- [76] Kim J-H, Kim D, Han HN, Barlat F, Lee M-G. Strain rate dependent tensile behavior of advanced high strength steels: experiment and constitutive modeling. Mater Sci Eng A 2013;559:222–31.
- [77] Weck A, Wilkinson DS. Experimental investigation of void coalescence in metallic sheets containing laser drilled holes. Acta Mater 2008;56:1774—84.